Plasma Chem Plasma Process (2006) 26:371–391
DOI 10.1007/s11090-006-9019-1

ORIGINAL ARTICLE

Phenomena Involved in Suspension Plasma Spraying Part 1: Suspension Injection and Behavior

J. Fazilleau · C. Delbos · V. Rat · J. F. Coudert · P. Fauchais · B. Pateyron

Received: 6 July 2005 / Accepted: 2 February 2006 /
Published online: 21 April 2006

Abstract Suspension Plasma Spraying (SPS) is a relatively new deposition process which enables to spray micron and submicron particles. It offers the possibility to form finely structured coatings with intermediate thicknesses of a few tens of microns. In order to have a better understanding in SPS, the two parts of this paper are devoted to the description of the phenomena involved in this spray process. The first part focuses on the suspension injection within a d.c. plasma jet. Simplified models, backed by plasma and suspension diagnostics, allow describing the interaction plasma-suspension. It is shown that the suspension is atomized by the plasma jet before the starting of the droplets vaporization. The plasma jet recovers its flow symmetry about 15 mm downstream of the nozzle exit. The strong influence of plasma instabilities on suspension injection is also highlighted. The second part is devoted to solid particle treatments and the coating formation.

Keywords d.c Plasma spraying · Suspension injection · Suspension droplets · Characteristic times · Droplets fragmentation · Plasma imaging · Voltage fluctuations

Nomenclature

C_D	Drag coefficient (-)
c_p	Specific heat of gas (J/kg·K)
c_{pl}	Specific heat of liquid (J/kg·K)
d_d	Droplet diameter resulting from drop fragmentation (m)
d_s	Initial suspension drop diameter (m)
F	Drag force (N)
F_G	Surface tension force (N)
H	Heat transfer coefficient (W/m^2·K)
H'	Heat transfer coefficient with corrections (W/m^2·K)

J. Fazilleau · C. Delbos · V. Rat (✉) · J. F. Coudert · P. Fauchais · B. Pateyron
Laboratoire Science des Procédés Céramiques et Traitements de Surface
Université de Limoges, UMR-CNRS 6638, conventionné avec le CEA n○ M08
87060 Limoges Cedex, France
e-mail: vincent.rat@unilim.fr

I Arc current (A)
L_v Enthalpy of vaporization of liquid (J/kg)
$\dot{m}$ Mass flow rate (kg/s)
m_s Mass of the drop (kg)
Nu Nusselt number $Nu = \frac{Hd_p}{\kappa}$ (-)
Pr Prandtl number $Pr = \frac{\mu c_p}{\kappa}$(-)
r_d Droplet radius (m)
r_s Initial drop radius (m)
Re Reynolds number $Re = \frac{\rho u d_p}{\mu}$(-)
t Time (s)
T Plasma temperature (K)
T_a Ambient temperature (K)
T_b Boiling temperature (K)
T_s Surface temperature of the liquid (K)
u Plasma velocity (m/s)
U Relative velocity plasma/drop $U = u - v$
V Arc voltage (V)
$\overline{V}$ Mean arc voltage (V)
V_s Drop volume (m^3)
v Drop velocity (m/s)
We Weber number of a suspension drop $We = \frac{\rho\, u^2\, d_p}{\sigma}$.

Greek symbols

ΔE_s Variation of surface energy (J)
η Torch thermal efficiency (-)
$\overline{\kappa}$ Mean integrated plasma gas thermal conductivity (W/m·K)
κ Plasma gas thermal conductivity (W/m·K)
μ Plasma gas molecular viscosity (Pa·s)
ρ Density of plasma gas (kg/m^3)
ρ_s Density of the drop (kg/m^3)
σ Surface tension of liquid (N/m)
τ_f Characteristic fragmentation time of drops (s)
τ_v Characteristic vaporization time (s)

Abbreviations

CFD Computer Fluid Dynamic
CVD Chemical Vapor Deposition
d.c. Direct Current
1D 1 Dimension

1. Introduction

Since the 1990 nanostructured materials are considered as a new concept for increasing the performance of engineering components. Research efforts have demonstrated that many

properties of nanostructured materials differ from conventional ones due to the large volume fraction of internal interfaces. There are several methods to produce nanoscale thin coatings (thickness $e < 2\mu$m) starting from gas phase such as reactive magnetron sputtering [1], chemical vapor deposition (CVD) [2], thermal plasma assisted CVD [3], hypersonic plasma particle deposition [4]. For thick coatings ($e > 100\mu$ m), many works have been recently devoted to the spraying (plasma or high velocity oxygen-fuel (HVOF) flame) of agglomerated nano-particles in a mushy state at impact [5–7] or made of materials with different melting points such as TiO_2 and Al_2O_3 [8–10]. At last, to fill the gap between thicknesses of 1–100 μm, techniques where a liquid is injected in a flame or a plasma have been developed. They comprise either a metal precursor: nitrates, isopropoxides, butoxides…dissolved in ethanol, isopropanol, *n*-butanol… or a suspension of nano or micron particles. In the first case, after the vaporization of the solvent, followed by the vaporization of the metal precursor with its possible reaction with the plasma gas, the coating is obtained by either CVD or the deposition of recondensed particles onto the substrate [11–15]. However, the coating resulting from the latter technique is usually in a powdered state because the impact velocity of particles is very low (a few ms). Thus, these coatings have to be consolidated for example by sintering, the sintering temperature of nanosized particles being often lower than that of microsized ones [16]. The second solution consists in injecting a suspension in a direct current (d.c.) plasma jet [17–25]. The aim is to fragment directly by the plasma jet the injected drops (a few hundreds of μm in diameter) into dispersed droplets, now only a few μm in diameter, vaporize the droplet solvent, heat and accelerate particles contained within droplets, and spray them, as in conventional plasma spraying (CPS), in a fully or semi-molten state onto the substrate. However, in this case, the size of the molten particles is between 0.1 and 3 μm and the resulting splats have diameters between 0.2 and 6 μm with thicknesses in the range 20–300 nm. The properties of coatings obtained are extremely sensitive to the process parameters [17–25]. The latters include the torch operating conditions, the arc root fluctuations, the size of the drops injected, their fragmentation into droplets by the d.c. fast plasma jet, the vaporization of the droplet solvent, the particle melting and acceleration, and the heat flux imposed by the plasma jet. The heat flux can be very important with spray distances which are only a few centimeters. Compared to CPS where, for example, with zirconia particles 20μm in diameter, about 10^8 particles per second are injected, with 1 μm diameter particles 10^{11} particles per second have to be considered. Besides, if now measuring techniques of a single particle parameters at impact (temperature, velocity, and diameter: at least over 10 μm) are well established, they cannot be used for particles with diameters below 1 μm. It seems however, that ensemble measurement techniques can give a good trend of the particle temperature evolution [26]. Thus, the main means available for a better understanding of this new process are modeling as well as splat and coating characterizations.

To understand what happens to the liquid particles, it is, of course, possible to develop computational fluid dynamic (CFD) complex calculations as did Kolman for d.c plasma jets [27] or Shan and Mostaghimi for radio frequency plasmas [28].

In this paper, it has been chosen to rise simple 0D or 1D equations and use, when necessary, parabolic 2D CFD models pointing out the key parameters controlling the process. In this first part, the suspension plasma spraying set-up developed will be briefly presented and the simple models used to determine, according to the torch working parameters, the velocity and temperature of the flow at the nozzle exit. These data allow calculating the characteristic times of droplet fragmentation and vaporization. The results obtained explain how the injected drops are first fragmented in micron sized droplets before they are vaporized. The calculations are backed by imaging and spectroscopic measurements. The second part of this paper, starting at the end of the droplet vaporization step, deals with:

– the heat and momentum transfer to the particles,
– the possible mechanisms occuring in the plasma for the splat formation in conjunction with the initial particle size distribution and morphology,
– the coating generation.

2. Experimental set-up

2.1. Plasma torch and suspension injection

The experimental set-up consists of a d.c. plasma torch (Sulzer Metco PTF4 type) and suspension feeders (Fig.1). The d.c. plasma torch was operated either with an Ar–H_2 (45/15 slm), or an Ar–He–H_2 (40/10/50 slm) or an Ar–He (40/80 slm) mixture as plasma forming gases and a 6 mm internal diameter anode nozzle (see Table 1). During all experiments, the torch time averaged characteristics (arc current and voltage, thermal efficiency, and plasma forming gas mass flow rates) were measured, the gas specific enthalpy was calculated and all these data were recorded with a specifically developed computer code. The working conditions used are summarized in Table 1. It has to be noted, in Table 1, that the specific enthalpy of the Ar/He/H_2 plasmas is higher than that of the Ar/H_2 one and, from measurements performed in other conditions as well as from the number of moles contained in both gases, it can be inferred that the mean plasma velocity is probably slightly higher with the ternary mixture than with the binary one. The Ar–He mixture with a high gas flow rate (120 slm) and a rather low enthalpy was mainly used to spray submicron particles to avoid their vaporization. For each spray conditions, the voltage time evolution was also recorded.

The injection system is composed of tanks, in which the suspensions are stored, and an injector consisting in a stainless steel tube with, at the tip, a calibrated injection hole 150 μm in internal diameter manufactured by electro-erosion. The suspension is mechanically injected by controlling, with compressed air, the pressure of the liquid in the tanks, pressure monitored with a gauge. The arrangement provides, for a given injection pressure, a unique size and velocity for the drops. Their size depends on the injection nozzle internal diameter while their velocity is linked to the pressure in the reservoir which can be adjusted to optimize the drop

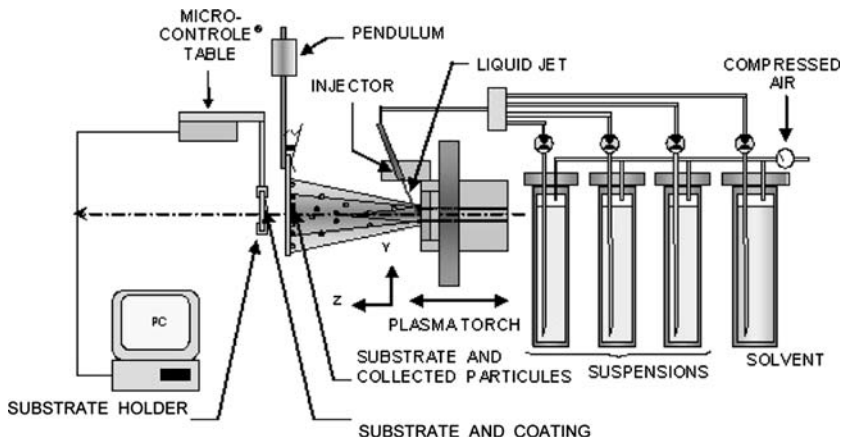

Fig. 1 Experimental set-up

Table 1 Spraying parameters

Internal nozzle diameter (mm)	Plasma gas composition	Arc current (Amps)	Mean arc voltage (V)	Mean specific enthalpy (MJ/kg)
6	Ar/H_2 (45/15 slm)	500	65	14.6
6	Ar/H_2/He (45/10/50 slm)	500	70	15.2
6	Ar/He (40/80 slm)	300	62	8.2

penetration within the plasma jet. The use of four tanks allows spraying simultaneously up to three suspensions and also to clean the injection nozzle before and after spraying by using the solvent contained in the fourth tank. The injector is accurately positioned with a four axes Micro-Contrôle® system permitting a reproducible injection. The injector axis is positioned in such a way that the flow of suspension drops penetrates the plasma at counter-flow and targets the nozzle axis at the exit of the nozzle (Fig.1). The angle of injection with respect to the nozzle axis is 60°. Two sets of optical lenses, orthogonal and parallel to the plane defined by the axis of injection and that of the plasma torch, allow to visualize on-line with a CCD camera the liquid penetration within the plasma jet and to adjust the injector position.

2.2. Powders

Two ceramic powders have been used, all of them being made of zirconia doped with 13 wt.% yttria (YSZ). The first one is provided by Tosoh Corp. (Japan). It has a specific surface area of 13 m^2/g and a mean crystallite size of 25 nm. The nanometric grains of the Tosoh powder agglomerate and aggregate resulting in a mean particle size in the suspension of 500 nm, the particles having finally a size ranging between 100 nm and 5 μm (Fig. 2a).

The second powder results from the attrition milling of fused and crushed particles initially between 22 and 45 μm in diameter. After wet milling during 13 h, the size distribution is between 0.8 and 3μm (Fig. 2b). Their volume and number size distributions will be presented in part 2. By using two powders, particle, and splat distributions will be then discussed.

2.3. Suspensions

The solvent used is ethanol. The suspension must have a low viscosity and a good stability to be compatible with the process. A suitable dispersant, which is adsorbed on the particle surface, allows for an effective dispersion of the particles in the solvent. The dispersant used

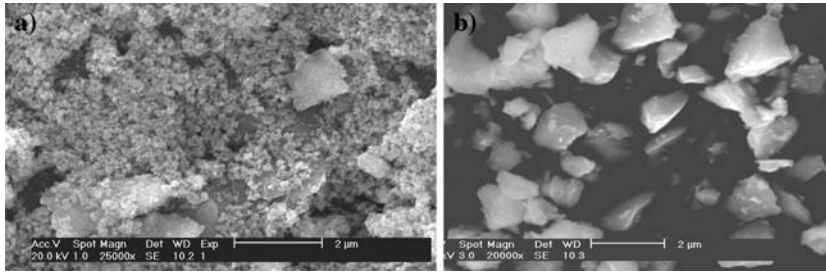

Fig. 2 Comparison of the morphologies of the YSZ powders used for the suspensions **(a)** commercial powder Tosoh and **(b)** attrition milled powder

is a phosphate ester. It acts by a combination of electrostatic and steric repulsions. For a detailed description of the way the suspension is prepared see references [22, 29].

The rheological studies, including viscosity measurements and sedimentation tests, showed that the YSZ suspensions with 13 wt.% of yttria and containing 2 wt.% (dispersant/powder) of dispersant displayed the minimum viscosity of 1.4 mPas with a shear-thinning behavior. It means that, when injecting the suspension at the right beginning of its interaction with the plasma when the shear stress imposed by the plasma flow is low, the suspension viscosity is high and then decreases drastically when the suspension penetrates within the plasma jet.

2.4. Measurement devices

Suspension plasma sraying was studied through:

- The drop injection by imaging the plasma jet and the drop trajectory with the CCD camera of the SprayWatch® system [30]. It uses a fast shutter camera and a filtered laser flash illumination at 808 nm allowing checking the good penetration of the suspension drops inside the plasma and choosing the optimal pressure of injection for a given liquid or suspension. It also allows visualizing the plasma jet fluctuations due to its arc root fluctuations.
- The perturbation of the plasma jet by the solvent using non-symmetrical emission spectroscopy [18].
- The particle momentum and heat transfer at impact by observing and characterizing (diameter and thickness) the resulting splats collected with glass or stainless steel lamellae disposed at the extremity of the pendulum (see Fig. 1); the splat number size distribution was also compared to that of the initial particles. The pendulum, on which a glass or stainless steel lamella is fixed, allows collecting in-flight particles at different distances (accuracy $\sim$ 1 mm) from the nozzle exit (Fig. 1). The pendulum velocity mainly depends on its mass, length, and the angle from which it is thrown. The maximum velocity of the substrate at the extremity of the pendulum is 3.2 m/s. By controlling its velocity and position, a lamella collects, at different distances downstream of the injection point, various quantities of splats resulting from the flattening and solidification of particles after their treatment in the plasma. Besides splats, spherical particles, and agglomerates were also collected. The formers result from melted and cooled particles (too long, spray distance) impacting in a mushy state, thus sticking to the substrate but keeping their shape or from recondensed vaporized small particles. The latters were collected at too short distances ($<$30 mm) corresponding to not yet melted agglomerates. The collecting time corresponded to a few milliseconds. The resulting samples were analyzed with a scanning electron microscope (SEM), an atomic force microscope (AFM) and an interferometric microscope (IM) in order to observe the morphologies of the collected splats, or sticking particles.
- The experimental set-up is also equipped with a X–Y displacement system to achieve coatings on button type samples (25 mm in diameter and 5 mm in thickness). As for the pendulum, the stand-off distance can be varied with the same accuracy. The resulting coating morphologies were studied by scanning electron microscopy.
- In order to measure the heat flux imposed by the plasma jet for short stand-off distances (down to 30 mm from the nozzle exit), a copper substrate, 30 mm in diameter and 10 mm in thickness, has been used. It was equipped with two thermocouples, one in its center and just below its surface and the other in its periphery, e.g. outside the area intercepting the plasma jet. From the local temperature measured at the substrate center and the heat

propagation time to reach a uniform temperature within the substrate, the heat flux can be calculated, provided that the width of the substrate area heated directly by the plasma jet was also measured.

3. Suspension injections

3.1. Imaging

Figure 3 shows, for three injection pressures, the suspension injection within a d.c. plasma jet generated at 500 A with the argon–hydrogen mixture (45/15 slm). The camera aperture time was 50μs and five laser pulses were generated with duration of 1μs. The pulse interval was 5 μs.

Two important points can be noticed in this figure:

- The penetration of the liquid jet increases with the injection pressure,
- As soon as the jet of drops (in the 220 μm in mean size) reaches the fringes of the plasma jet, drops start to be atomized. The fragmentation of the drops into smaller droplets seems to occur before their vaporization takes place. This is confirmed by the two orthogonal pictures of the jet taken with a CCD camera with suspension injection and shown in Fig. 4. The image orthogonal to the injector and plasma jet axis (exposure time of 10^{-4} s) shows an almost symmetrical jet, slightly deviated to the opposite of the injection. The image parallel to that plane shows that the jet is separated into two parts as close as 5 mm downstream of the nozzle exit.
- Plasma jets produced with Ar–H_2 and Ar–He–H_2 mixtures fluctuate according to the restrike mode [31] and the most important fluctuations are observed with the Ar–H_2 plasma. The voltage in these conditions can vary by $\pm$30 V around its mean value $\overline{V}$ corresponding to a ratio $\Delta V / \overline{V} = 46\%$. It means that the drops, regularly injected, are submitted to a plasma jet fluctuating in length and position with very different momenta. This is shown in Fig. 5, where it can be seen that the penetration and fragmentation are closely linked to the plasma jet instant parameters. The pictures of Fig. 5 have been obtained for the same experimental conditions but at different instants. Each picture corresponds to two laser pulses separated by 5 μs. In this case, the drops are clearly separated.

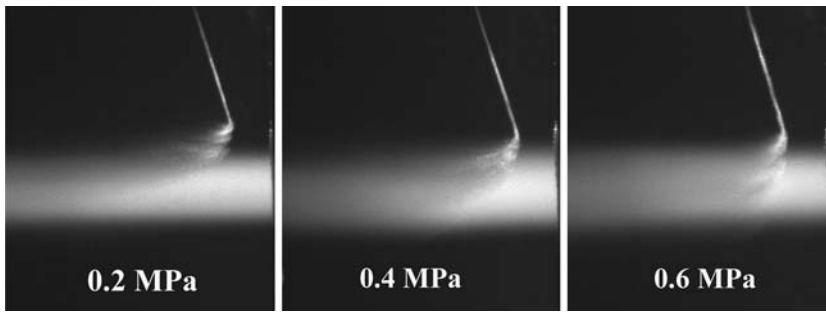

Fig. 3 Liquid injection photographies with SprayWatch system for three injection pressures (Ar–H_2 plasma see Table 1)

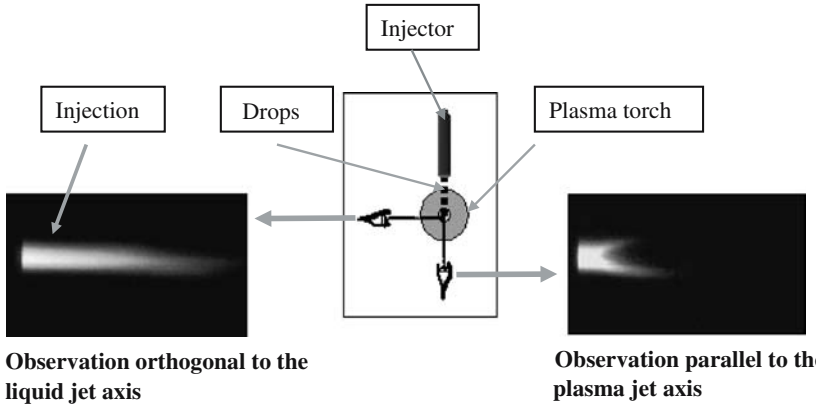

Fig. 4 The CCD camera pictures of the liquid–plasma interaction (shutter time 10^{-4} s, Ar–H_2 plasma, see Table 1)

Fig. 5 Influence of the arc fluctuations on drops penetration in the Ar–H_2 plasma jet

3.2. Emission spectroscopy

The images shown in Fig. 4 were comforted by emission spectroscopy measurements when injecting water instead of suspension [18]. Water was injected with a 3.6×10^{-4} kg/s mass flow rate in the plasma jet. This mass flow rate corresponds to that obtained with the optimum pressure to achieve a good penetration in the Ar–H_2 plasma jet (see spraying parameters in Table 1). Water instead of ethanol was chosen because, in the first 10–15 mm of the plasma jet, almost no oxygen from the surrounding air could be detected (about 2 vol.% at 20 mm in similar working conditions [32]). Thus, oxygen measured from the oxygen atomic lines emitted is that resulting from the injected water. On the contrary with ethanol, oxygen, hydrogen, and carbon are injected making the interpretation of spectroscopic measurements more difficult. A water suspension could also have been used instead of pure water but the spectroscopic measurement interpretation with the presence of tiny particles would have been more complex. As with the suspension, results similar to those presented in Fig. 4 were obtained, the jet being divided into two parts as shown by the shape of temperature isocontours (Fig. 6) measured at 5 mm downstream the nozzle exit.

However, at $z = 15$ mm, the temperature maximum is again located on the plasma jet axis. It means that the water, initially injected, has been completely vaporized, the vapor dissoci-

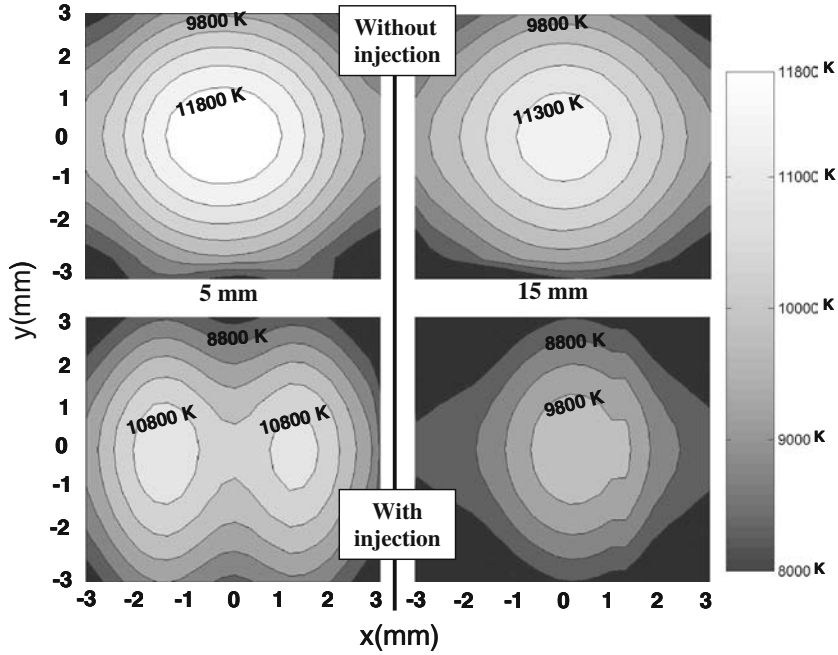

Fig. 6 Spectroscopic measurements of temperature without and with water injection (22 mL/min) (Ar–H_2 plasma jet which characteristic are given in Table 1)

ated in oxygen and hydrogen atoms, which at that distance are fully mixed with the plasma, which is again homogeneous. Such measurements are based on the Local Thermodynamic Equilibrium (LTE) assumption [18] which is not likely adequate in the area where water is vaporized, but they confirm the pictures shown in Fig. 4.

This spectroscopic investigation highlighted that a large part of the plasma enthalpy is still available to treat the solid particles 15 mm downstream of the liquid injection point, in case of water injection. Figure 7 represents the calculated specific enthalpy of an Ar–H_2 plasma jet and that of two mixtures Ar–H_2-H_2O corresponding, respectively, to the mass fractions given in Table 2. The injected water flow rate corresponds to some intermediate value between both mixtures with water. For the enthalpy dissipated in the pure Ar–H_2 plasma jet and corresponding to a mean plasma temperature of 13,000 K (see Fig. 7), both mixtures with water result in temperatures, respectively, of 11,700 and 10,500 K. The temperature of 11,000 K observed 15 mm downstream of the nozzle exit (Fig. 6) is in good agreement with this simplified calculation. It means that, after the suspension vaporization and the resulting vapor heating, a lot of energy is still available to melt the solid particles dispersed into fragmented droplets. Of course, when ethanol is used instead of water, the available specific enthalpy is slightly higher, the liquid vaporization requiring 3.2 less energy with ethanol than with water as shown in Table 3. However, most of the energy lost by the plasma with the solvent injection is linked to its dissociation and components ionization.

In principle, the combustion of ethanol can bring an important heat quantity further downstream when combustion could occur with the entrained oxygen. This combustion could compensate the energy lost by heating and vaporizing. Döring et al. [33] noticed, at a distance of 80 mm, an increase of temperature and speed when injecting ethanol in an Ar–H_2plasma

Table 2 Mass fractions of the different plasma mixtures used for the calculation of the specific enthalpy in Fig. 7

Mass fraction	Ar–H_2	Ar–H_2-H_2O	Ar–H_2-H_2O
Ar	0.984	0.850	0.750
H	0.016	0.030	0.040
O	0.000	0.120	0.210

Table 3 Comparison of water and ethanol vaporization

	Water	Ethanol
Boiling temperature T_b (K)	373	351
Surface tension σ (N/m) at T_a	72×10^{-3}	22×10^{-3}
Specific heat c_{pl}(J/kg·K) at T_a	4.2×10^{3}	2.4×10^{3}
Latent heat L_v (J/kg)	2.3×10^{6}	0.9×10^{6}
Enthalpy of vaporization: $L_v + c_{pl}\cdot(T_b - T_a)$ (J/kg)	2.6×10^{6}	0.8×10^{6}

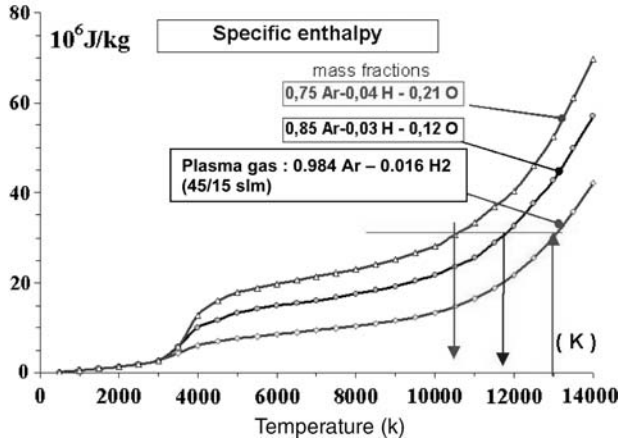

Fig. 7 Temperature dependence of the calculated specific enthalpy of Ar–H_2 (45–15 slm) and Ar–H_2–H_2O with mass fractions given in Table 2.

jet. Combustion enthalpy of ethanol is 29.8×10^3 kJ/kg, against 0.84×10^3 J/kg for its vaporization enthalpy. However, in the present experiments, at distances between 30 and 50 mm downstream of the nozzle exit, little oxygen (less than a few percents) is available [32] and combustion would only be possible further downstream because the injection takes place a few millimeters downstream of the nozzle exit. For particle treatment, this phenomenon is probably negligible because spray distances are between 30 and 50 mm.

4. Drops and droplets fragmentation and vaporization

In conventional plasma spraying, the particle cross-section on which acts the plasma (through its local pressure ρu^2) is constant during the particle injection while the suspension drop size continuously varies (Fig. 3). Studies of liquid drop breakup mechanisms, as in fuel atomization process, show that fragmentation is a complex phenomenon and different breakup regimes exist depending on the Weber number $We = \rho U^2 d_d/\sigma$. In the plasma core,

$We \sim 300$ and breakup should happen according to the catastrophic regime where Rayleigh–Taylor and Kelvin–Helmholtz waves are implied at different stages of the drop destruction [34]. However, it has to be noted that plasma properties (specific enthalpy and velocity as well as transport properties) continuously and drastically vary from the fringes of the plasma jet to its core leading to a continuous variation of the Weber number.

In a first crude approximation, the quantity ρu is almost constant along the plasma jet radius: in its fringes, u is low (a few hundreds of ms) but ρ is high, while, in the jet center, it is the reverse. Thus, the shear stress (ρu^2) applied by the plasma varies almost as u and increases drastically when droplets approaches the jet axis. However, the resistance of the droplets to this shear stress, varying as σ/d_d, increases because d_d decreases. Thus, it can be assumed that the shearing process of the droplets along their penetration in the plasma jet is self-adaptative. It is worth underlining that, in the following, the variation of σ with temperature has been neglected because it is only about 20% for ethanol between room temperature and its vaporization temperature.

4.1. Simplified plasma jet modeling

In order to evaluate the trends of the fragmentation and vaporization of droplets, a simple 2D stationary computational fluid dynamic code has been used where the inlet variables are the plasma jet enthalpy and its mass flow rate.

The mass flow rate is measured and the specific enthalpy $\overline{h}$ is calculated from the following equation:

$$\overline{h} = \eta \frac{\overline{V} I}{\dot{m}}, \tag{1}$$

where η is the torch thermal efficiency, $\overline{V}$ the mean arc voltage, I the arc current intensity, and $\dot{m}$ is the mass flow rate of plasma gases.

In these models, the thermodynamic and transport properties of plasmas are a prerequisite. They have been calculated at LTE [35] using mixing rules to account for the mixing of the plasma jet with the surrounding air or the solvent injected. The model Jet & Poudres used [36] is assumed to be axi-symmetric, steady and parabolic without swirl component. It is derived from the Genmix algorithm [37] and the mixing length [38] is used to describe the turbulence. However, the length of turbulence proposed by Genmix has been corrected to account for the specificity of the plasma flow:

- It is set at zero as soon as the temperature is over 8,000 K; where the jet is assumed to be fully laminar,
- The mixing length is written $\ell = 0.03\ell_s$ where ℓ_s is the distance between the calculation point and the torch axis at the nozzle exit. The coefficient 0.03 has been chosen in such a way the axial temperature distribution matches with the spectroscopic measurements of the jet,
- The molecular Prandtl number correlating the flow and the heat transfer is calculated at each temperature. For example, with the Ar–H_2 plasma (see Table 1) flowing in air, it varies between 0.15 and 0.78 all over the jet,

To represent the "cold" gas layer surrounding the plasma jet at the nozzle exit (see Fig. 3), the calculations are started inside a ficticious nozzle which length is assumed to be 5 mm. The thermal losses due to the cooling water vary linearly with the distance z and are 1,200 Wcm as measured when lengthening the torch nozzle [39]. It is assumed that, at the beginning of

the nozzle, the initial temperature and velocity radial profiles are flat. These profiles are then calculated along the torch axis in such a way that they are matched with the measured specific enthalpy (Eq. 1) and mass flow rate. The maximum temperature allowed in the calculations is limited to that spectroscopically measured at the nozzle exit increased by 500 K.

If the calculations with the Ar–H_2 plasma jet are straightforward, those with the same plasma jet where water or ethanol are injected cannot be performed because the jet is no more axi-symmetric (see Fig. 4) at least up to 15 mm downstream of the nozzle exit. However, what is important for the understanding of the heat and momentum transfer between the plasma and solid particles of the suspension is what happens once the plasma is again axi-symmetric 15 mm downstream of the nozzle exit (once the solvent is fully evaporated). Consequently, it has been assumed that the plasma jet temperature and velocity distributions at 15 mm and farther downstream are those resulting from an axi-symmetrical plasma jet obtained with a mixture of Ar–H_2–O_2 with the same specific enthalpy as that of the Ar–H_2 plasma. The mean momentum of the Ar–H_2 plasma jet has been supposed to be conserved with the Ar–H_2–O_2 plasma. As the mass of the latter is higher, it results in a lower velocity of this plasma. The thermodynamic and transport properties are those of the Ar–H_2–O_2-air outside the nozzle. Of course, such calculations can only give trends for the energy transfer between the plasma and solid particles contained within the droplets which, according to our assumption, starts farther than 15 mm downstream of the nozzle exit.

Figure 8 represents the axial temperature (a) and velocity (b) for Ar–H_2 and Ar–H_2–O_2 plasmas, flowing in air. In good agreement with the specific enthalpy evolution (see Fig. 7), the axial temperatures of the Ar–H_2–O_2 plasma jet are lower than those of the Ar–H_2 one (Fig. 8a) and they decrease faster along the jet axis due to the dissociation and ionization of oxygen. For the Ar–H_2–O_2 plasma at 15 mm (Fig.8a), the temperature axial distribution is rather close to that measured and presented in Fig. 6. As it could be expected, the axial velocity of the jet is lower than that of the Ar–H_2 plasma according to our assumption of momentum conservation (Fig. 8b).

Besides, calculations have been performed for a stationary plasma jet with the same arc current (500 A), same thermal efficiency (0.61), and either 35 or 95 V corresponding to the extrema of voltage fluctuations in order to determine their influence on the plasma jet temperature and velocity distributions. Figure 8 represents the corresponding axial temperatures (Fig. 8a) and velocities (Fig. 8b) of the plasma flowing in air. They show the drastic influence of voltage fluctuations especially at the extremity of the jet core, i.e. where temperature is about 8,000 K. A similar effect can be observed for the radial distribution 3 mm downstream of the nozzle exit (see Fig. 9). The jet radius decreases with the voltage. The values obtained for the stationary plasma are in good agreement with the spectroscopic measurements and the maximum velocity is close to that measured by Planche [40] in similar conditions.

4.2. Fragmentation and vaporization of suspension drops in the plasma jet

There are two main forces exerting on the drop entering into the plasma: drag force and surface tension force. A simple calculation to evaluate these forces shows that the drag force is two orders of magnitude higher than the surface tension one so it can be surely assumed that, in the experimental conditions described, the fragmentation of drops into droplets is very fast.

Our goal being to determine orders of magnitude for what happens to a suspension drop entering a plasma jet, a very simple approach has been considered in the following.

The size d_d of the tiny droplets resulting from a drop fragmentation is estimated by writing the equilibrium between aerodynamic and surface tension forces.

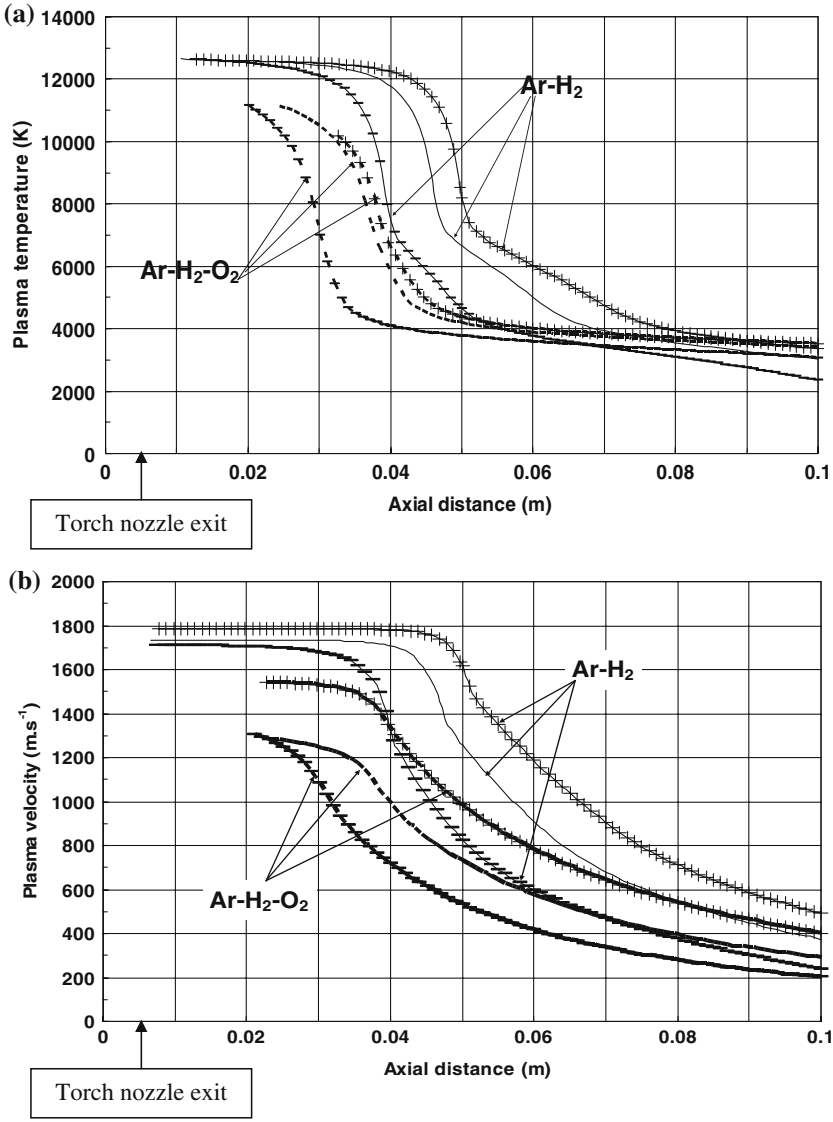

Fig. 8 Axial temperature **(a)** and velocity **(b)** profiles for the Ar–H_2 and Ar–H_2–O_2 plasma jets flowing in air. The profiles have been represented outside the nozzle exit for Ar–H_2 and 15 mm downstream for the Ar–H_2–O_2 (where the jet has recovered its axial symmetry). The curves + correspond to the maximum voltage (95 V), while those with—are related to the minimum voltage (35 V). *Full lines* are related to the mean voltage (65 V) for the Ar–H_2. For Ar–H_2–O_2, the same conventions have been used but with *dotted lines* instead of full ones

The drag force can be written:

$$F = \frac{\pi}{8} C_D d_d^2 \rho u^2, \tag{2}$$

where C_D is the drag coefficient and u is the velocity of the plasma jet. It has been assumed that the drop velocity is negligible compared to that of the plasma jet (a drop penetrates the plasma jet with a velocity of about 20 ms with 0.4 MPa injection pressure).

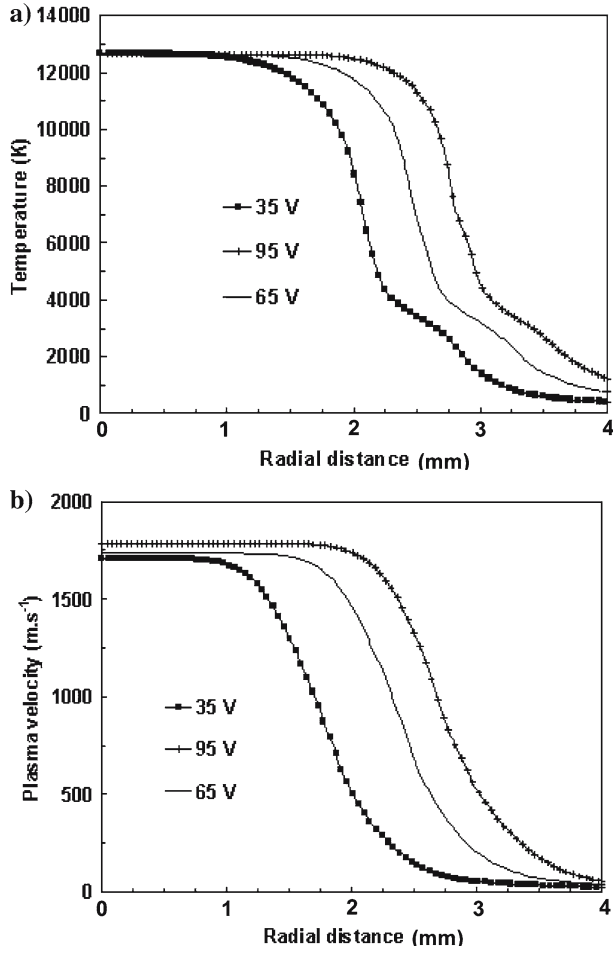

Fig. 9 Radial profiles of temperature **(a)** and velocity **(b)** for the Ar–H_2 plasma 3 mm downstream of the nozzle exit for three plasma torch voltage 35, 95, and 65 V. *Full lines* correspond to the stationary plasma ($V = 65$ V, $I = 500$ A)

The surface tension force is written:

$$F_G = \pi d_d \sigma, \tag{3}$$

where σ is the surface tension of the ethanol ($\sigma = 22 \times 10^{-3}$ Nm).

By equating Eqs. (3) and (4), it can be deduced that the minimum droplet diameter, when the fragmentation is completed, can be written:

$$d_d = \frac{8\sigma}{C_D \rho u^2}. \tag{4}$$

The calculation of the drop fragmentation has been performed along its mean trajectory taking into account the plasma temperatures and velocities seen by it. The starting drop diameter is an average of drop size measurements performed by using a CCD camera, e.g. 220 μm. The results are summarized in Fig. 10. However, it should be kept in mind that these calculations ignore the plasma jet cooling when fragmentation and vaporization take place. Thus, the drop diameter decrease along the plasma jet radius is overestimated.

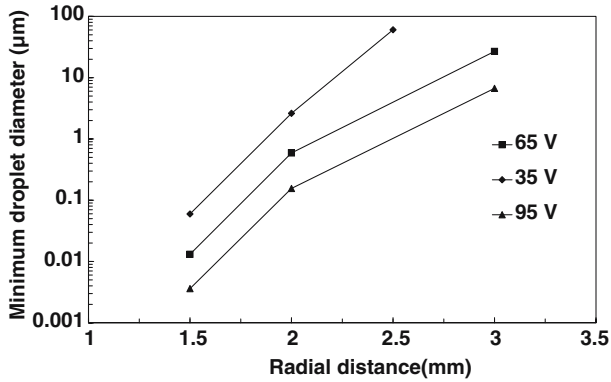

Fig. 10 Evolution of the ethanol drop diameter along the jet radius upon penetration within the Ar–H_2 plasma jet for the anode nozzle 6 mm in internal diameter at 3 mm from the nozzle exit for 3 V levels of the plasma torch, 35, 65, and 95 V

It can be readily seen that, in the plasma jet fringes, the drop diameter starts to be reduced as confirmed by the interaction of the liquid drop jet and the "cold" gas (see Fig. 3) and the resulting droplets are very rapidly decreasing in size. Of course, as it will be shown when considering vaporization, this calculation is correct as long as vaporization can be neglected, as it assumes that it occurs after fragmentation is completed. This calculation is no more valid for droplets with a diameter below 1 μm. According to Fig. 10, at a radius of about 2 mm, the initial drops are completely fragmented. However, two points have not been taken into account:

- Once the droplets start to vaporize, the plasma jet is cooled (see Figs. 4, 6) and slowed down which delay the fragmentation.
- The plasma jet fluctuations: when the voltage is 30 V lower than the mean value $\overline{V} = 65$V, the energy dissipated within it is almost twice less [41] thus reducing drastically the fragmentation. That is probably the reason why, in Fig. 5, slight deflection by droplets can be observed beyond the plasma jet axis. The influence of the voltage fluctuations is also shown in Fig. 10, where the minimum droplet diameter has been calculated for plasma torch voltages of 95 and 35 V. It can be observed that, at a fixed radial distance, the droplet diameter logically decreases as the plasma torch voltage, and therefore, the torch power, increase. For 35 V, the initial drop (220 μm in diameter) is not fragmented at a radial distance of 3 mm; this fragmentation starts at a radial distance of about 2 mm. Finally, it can be expected a strong influence of voltage fluctuations on droplet trajectories within the plasma jet and therefore, on the heat and momentum transfers between solid particles and the plasma jet.

Moreover, the times of fragmentation and vaporization for the initial drop of suspension entering into the plasma have been estimated.

It is considered that the suspension drop of radius r_s is fragmented into n droplets of radius r_d. The mass conservation obviously imposes that $r_s^3 = nr_d^3$. Moreover, the variation of surface energy, for a liquid of surface tension σ, during the step of fragmentation is written:

$$\Delta E_s = \sigma 4\pi (nr_d^2 - r_s^2) = \sigma 4\pi r_s^2 \left(\frac{r_s}{r_d} - 1 \right). \tag{5}$$

The work of the drag force F applied to the suspension drop of radius r_s can be simply written

$$W_f = FU\tau_f, \tag{6}$$

where τ_f is the fragmentation time of the drop. It is equal to the variation of surface energy, so τ_f can be calculated by writing:

$$\tau_f = \frac{8\sigma\left(\frac{r_s}{r_d} - 1\right)}{C_D\,\rho U^3}. \tag{7}$$

It is interesting to compare this characteristic time with that required to vaporize the drop entering the plasma jet. A simple analysis of the problem is to consider the equality between the heat flux transferred from the plasma to the drop and that absorbed by the drop during the time dt.

The heat flux, ϕ_1, transferred by convection from the plasma to the drop can be written :

$$\Phi_1 = 4\pi r_s^2 H(T - T_s), \tag{8}$$

where H is the convection coefficient (W/m^{2}K) written as follows:

$$H = \frac{\overline{\kappa} Nu}{2r_s}, \tag{9}$$

where $\overline{\kappa}$ is the mean thermal conductivity (W/mK), Nu the Nusselt number of the plasma, T the plasma temperature (K), and T_s is the temperature at the surface of the liquid, considered to be its vaporization temperature (K).

According to the Ranz–Marshall correlation, the Nusselt number is written:

$$Nu = 2 + 0.6 \cdot Pr^{1/3} \cdot Re^{1/2}, \quad Re < 200, \tag{10}$$

where Pr and Re are, respectively, the Prandtl and the Reynolds numbers.

The heat flux Φ_2 absorbed during the time dt by the fraction of the drop comprised between the radii r_s and $r_s + dr_s$ is written:

$$\Phi_2 = L_v \frac{dm_s}{dt} = L_v \rho_s \frac{dV_s}{dt}, \tag{11}$$

where L_v is the latent heat of vaporization of the liquid (J/kg), m_s the mass of the drop (kg), and ρ_s is the density of the drop (kg/m^3). The volume of the drop is V_s. Note that the heating of the liquid to the vaporization temperature can be neglected. The time variation of the volume of the drop V_s satisfies the following relationship:

$$\frac{dV_s}{dt} = 4\pi r_s^2 \frac{dr_s}{dt}. \tag{12}$$

The equality between both heat fluxes, with $dr_s/dt < 0$, results in:

$$4\pi r_s^2 H\,(T - T_s) = L_v \rho_s 4\pi r_s^2 \frac{dr_s}{dt}. \tag{13}$$

If it is assumed that, during the vaporization time τ_v, the drop radius varies from r_s to 0, then the vaporization time τ_v can de deduced:

$$\tau_v = \frac{L_v \rho_s\, r_s^2}{(T - T_s)\,\kappa Nu} \tag{14}$$

Of course, due to the strong evaporation of the droplets, the Nusselt number has to be corrected by the effects of rarefaction (Knudsen effect) and vapor buffer formed around the droplet, resulting in a modified heat transfer coefficient H'. The corrections proposed by Pfender [42] for the former and by Borgianni et al. [43] for the latter have been used (the

correction of Borgianni et al. has also been used in plasma conditions as proposed by Chen and Pfender [44].

Figure 11 shows a comparison between the fragmentation and the vaporization times as function of the droplet diameter for the stationary plasma ($\overline{V} = 65\,\mathrm{V}$) . The attention of the reader must be drawn to the fact that, in Fig. 11, the vertical scale is logarithmic. Thus, over $1\,\mu$m droplet diameters, the fragmentation times are at least two orders of magnitude lower than the vaporization times. This difference is increased when the vapor buffer effect is taken into account.

These very short times of drop fragmentation followed by the droplet vaporization explain the emission spectroscopy results presented in Fig. 6 and showing that, 15 mm downstream of the nozzle exit, the plasma jet has recovered its axial symmetry. At that distance, all the solvent is vaporized and its components uniformly mixed with the plasma jet which is now an Ar–O–H plasma (when the solvent is water).

4.3. Fragmentation and evaporation of drops in the fringes of the plasma jet

As shown in Fig. 3, fragmentation starts in the plasma jet fringes induced by the "cold" ($T \sim 2,000$–$4,000\,\mathrm{K}$) flow surrounding the plasma jet at the nozzle exit. As it can be seen from this figure, some fragmented drops do not penetrate into the jet core and are entrained in its fringes. This phenomenon is enhanced by the plasma jet fluctuations as shown in Fig. 5. It is thus important to determine what will happen to these drops: will they impact as liquid droplets on the substrate or will the solvent be completely evaporated before the particles contained in droplets impact on it?

To be in the worst conditions, it has been assumed that the droplets fragmented in the jet fringes are about $50\,\mu$m in diameter (see Fig. 10), and travel parallel to the jet axis at 3 mm from it. This distance is about that where the liquid drops start to be fragmented by the "colder" gas flowing in the plasma jet boundary (see Fig. 3). Using the temperature and velocity distributions caculated by the Jet & Poudres code [36] for the Ar–H_2 plasma jet, the fragmentation and vaporization times of these droplets have been calculated and they are presented in Fig. 12 for the stationary plasma ($\overline{V} = 65\,\mathrm{V}$). The latter shows that the droplets are fragmented and the temperatures along this trajectory in the jet fringes are largely sufficient to vaporize the drops very rapidly, in a few tenths of millimeters trajectory. The problem is then what will happen to the small solid particles contained in the vaporized droplets. Tentative calculations (see description in part 2) have shown that these particles with the initial velocities relatively parallel to the jet axis are in most cases pushed out of the hot zones by

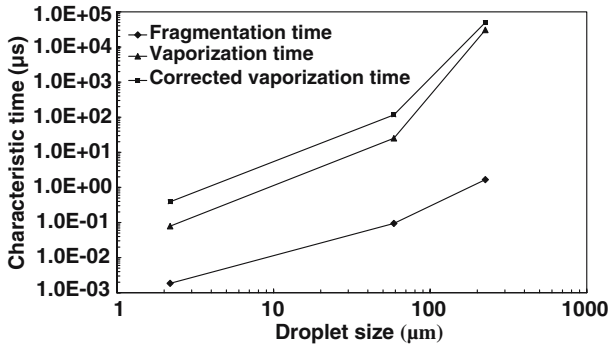

Fig. 11 Evolution of fragmentation and vaporization times of ethanol droplets as function of the minimum droplet diameter without and with correction due to the buffer effect of the vapor cloud around droplets for the stationary ($\overline{V} = 65\,\mathrm{V}$) Ar–$H_2$ plasma jet

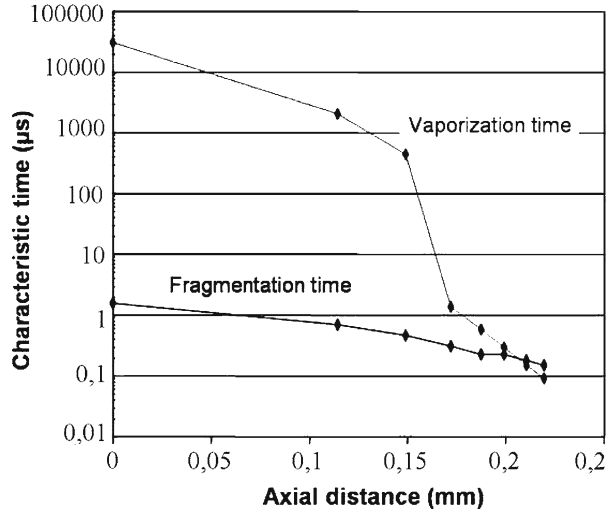

Fig. 12 Fragmentation times of a 50 μm ethanol drop travelling parallel to the jet axis at 3 mm from it calculated for the stationary ($\overline{V} = 65$ V) Ar–H_2 plasma jet

the thermophoresis effect and in most cases are not melted. This is confirmed by the dust cloud around the substrate, which can reduce the coating quality when embedded within it.

4.4. Comparison between pure ethanol and suspension

All previous calculations were performed with pure ethanol for which the data are available. However, when injecting the suspension in the same plasma jet, the behavior is slightly different as shown in Fig. 13.

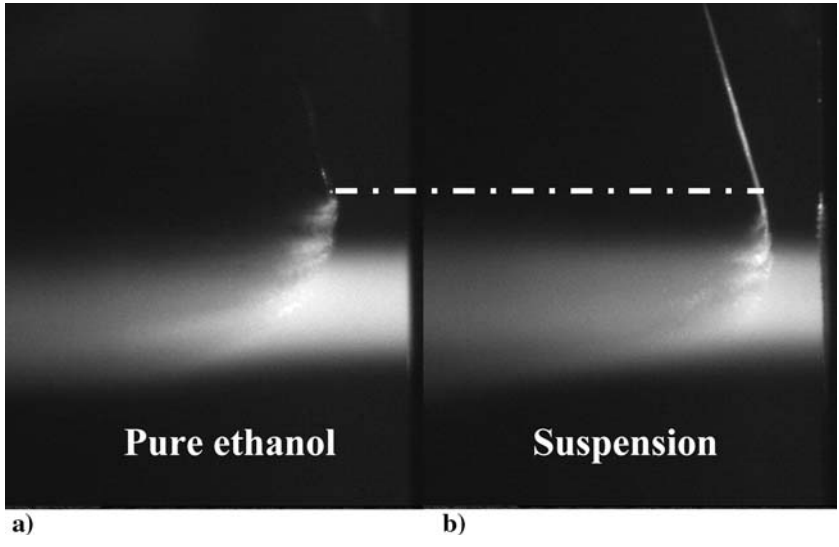

Fig. 13 Influence of the liquid jet composition on its fragmentation by the the Ar–H_2 d.c. plasma jet: **a** pure ethanol and **b** suspension. Pictures taken with the SprayWatch: exposure time 50 μs, five laser flashes of 1μs duration with a delay of 5 μs between each

This difference of behavior, at least, in the jet fringes, is probably due to the shear-thinning behavior of the suspension. When the shear stress imposed by the momentum of the plasma jet is low, the viscosity is very high. However, it drops rapidly to 1.4 mPa s which is close to that of pure ethanol (1.2 mPa s). To perform the calculations with the suspension, its properties, such as surface tension, should be determined, which was unfortunately not the case. However, Fig. 13 shows that the trend, i.e. fragmentation followed by vaporization, is the same as with ethanol, which is confirmed by the jet images (see Fig. 4).

5. Conclusion

A new process, the suspension d.c. plasma spraying (SPS), has been developed where suspensions of particles (micron or submicron sizes) are mechanically injected in a d.c. plasma jet. The advantage of the mechanical injection compared to atomization is threefold:

- It avoids the plasma jet perturbation by the atomization gas,
- It allows injecting calibrated drops (in the experiments described about 220 μm in mean diameter) with a given velocity, no dispersion of droplet trajectories and sizes as in the gas atomization process,
- The use of an accurate positioning system of the injector allows injecting precisely the drops at the chosen location.

The study of the injection by using a CCD camera coupled with a laser flash has shown that the drops are fragmented into smaller droplets as soon as they penetrate into the plasma jet fringes (by the "cold" flow surrounding the plasma column in the anode-nozzle). This fragmentation increases drastically with the further penetration of the already fragmented droplets into the plasma jet itself.

Simplified calculation of characteristic times of momentum and heat transfer between drops, and then droplets of the solvent, and the plasma jet have shown that, for ethanol as solvent, the fragmentation time is at least two orders of magnitude shorter than that of vaporization, at least for droplets with sizes over 0.5 μm. Thus, it can be assumed that fragmentation, which takes a few μs, is completed long before vaporization which becomes rather fast only for droplets below a few μm in diameter. Such results are confirmed by spectroscopic measurements, made with the pure solvent (water for these measurements) and have shown that, for the Ar–H_2 plasma jet used, at 5 mm downstream of the nozzle exit, the jet is cut into two parts when the suspension is injected (with two maxima off-axis) by the suspension vaporization. However, 15 mm dowstream the nozzle, the plasma jet has recovered its symmetry and the components of the solvent are homogeneously mixed with the plasma gas. Measurements and simplified flow calculations have also emphasized the drastic effect on drop fragmentation of the voltage fluctuations ($\pm$30 V for a mean voltage of 65 V with an Ar–H_2 plasma working in the restrike mode). These fluctuations, in the 200 μs time range, induce important plasma jet velocity variations which accelerate or delay the fragmentation, occurring in the μs time range, when the voltage increases or decreases. These phenomena probably play a key role on the coating formation and more precise studies are to be made on them in the future.

Finally, when injecting a suspension, even though its rheological behavior is slightly different from that of pure ethanol in the jet fringes, it can be assumed that the big drops ($\sim$ 220 μm) are fragmented in a few microseconds in droplets with sizes below a few micrometers. These droplets are then completely vaporized and the solid particles contained in them are released after 10–15 mm trajectories in the plasma jet.

The second part will detail how they are accelerated and heated, how they flatten onto the substrate to form splats, which layering form the coating. The properties of the latter are also linked to the transient high-heat flux (up to 20 MWm^2) imposed by the plasma jet to the coating in formation.

References

1. Zhang S, Sun D, Fu Y, Du H (2003) Surf Coatings Technol 167:113
2. Choy KL (2003) Prog Mater Sci 48:57
3. Lu SP, Heberlein J, Pfender E. (1992) Plasma Chem Plasma Proc 12:35
4. Heberlein J, Portel O, Girshick S, McMurry P, Gerberich W, Iordanoglou D, Difonzo F, Neumann D, Gidwani A, Fan M, Tymiak N (2001) Surf Coatings Technol 142-144:265
5. Lima RS, Kucuk A, Berndt CC (2001) Surf Coatings Technol 135:166
6. Zeng Y, Lu SW, Gao L, Ding CX (2002) J Eur Ceramic Soc. 22:347
7. Chen, H, Ding CX (2002) Surf Coatings Technol 150:31
8. Shaw L, Goberman D, Ren R, Gell M (2000) Surf Coatings Technol 130:1
9. Gell M, Jordan EK, Sohn YH, Goberman D, Shaw L, Xiao TD (2001) Surf Coatings Technol 146–147:48
10. Karthikeyan J, Berndt CC, Tikkanen J, Wang JY, King AH, Herman H (1997) Nanostruct Mater 8:61
11. Karthikeyan J, Berndt CC, Tikkanen J, Wang JY, King AH, Herman H (1997) Nanostruct Mater 9:137
12. Bouyer E, Gitzhofer F, Boulos MI (1997) In: Fauchais P (ed) Progress in plasma processing of materials, Begell House, NY, USA, p 735
13. Bouyer E, Müller M, Dignard N, Gitzhofer F, Boulos MI (1997) In: Fauchais P (ed) Progress in plasma processing of materials, Begell House, NY, USA, p 751
14. Bouyer E, Branston DW, Lins G, Müller M, Verleger J, von Bradke M (2001) In: Fauchais P (ed) Progress in plasma processing of materials Begell House, NY, USA, p 501
15. Yang GJ, Li CJ, Han F, Mav SF (2003) In: Moreau C, Marple B (eds) Thermal spray 2003: advancing the science and applying the technology, ASM Int. Materials Park, OH, USA, p 675
16. Yang G, Zhang H, Biswas P (1996) Nanostruct Mater 7:675
17. Blazdell P, Kuroda S (2000) Surf Coatings Technol 123:239
18. Wittmann K, Blein F, Coudert JF, Fauchais P (2001) In: Berndt CC, Khor KA, Lugscheider (eds) Thermal spray: new surfaces for a new millenium, ASM Int. Materials Park, OH, USA, p 375
19. Gitzhofer F, Bonneau ME, Boulos MI (2001) In: Berndt CC, Khor KA, Lugscheider (eds)Thermal spray: new surfaces for a new millenium, ASM Int. Materials Park, OH, USA, p 61
20. Wittmann K, Fazilleau J, Coudert JF, Fauchais P, Blein F (2002) In: Lugscheider E (ed) Proceedings of ITSC 2002, DVS, Düsseldorf, Germany, p 519
21. Kuroda S, Blazdell P (2002) In: Lugsheider E (ed) ITSC2002 proceedings, DVS, Dusseldorf, Germany, p 539
22. Fazilleau J, Delbos C, Violier M, Coudert JF, Fauchais P, Bianchi L, Wittmann-Ténèze K (2003) In: Moreau C, Marple B (eds) Thermal spray 2003: advancing the science and applying the technology, ASM Int. Materials Park OH, US, p 889
23. Delbos C, Fazilleau J, Coudert JF, Fauchais P, Bianchi L, Wittmann-Ténèze K (2003) In: Moreau C, Marple B Thermal (eds) Spray 2003: advancing the science and applying the technology, ASM Int. Materials Park, OH, US, p 661
24. Fazilleau J, Delbos C, Coudert JF, Fauchais P, Denoirjean A, Bianchi L, Wittmann-Ténèze K (2003) In: d'Agostino R (ed) 16th international symposium on plasma chemistry (electronic version), University of Bari, Italy
25. Delbos C, Fazilleau J, Rat V, Coudert JF, Fauchais P, Bianchi L (2004) In: Proceedings of ITSC 2004, DVS, Düsseldorf, Germany (electronic version)
26. Moreau C (2004) Advanced particle diagnostics for controlling plasma spray processes. In: Proceedings of sensors and controls 2004 Boucherville, CN, Oct 26–27. CNRC Industrial Materials Institute, Boucherville, CN
27. Kolman D (1997) Thesis, Ph.D. University of Minnesota, Minneapolis
28. Shan Y, Mosthagimi J (2003) In: Thermal Spray 2003: advancing the science and applying the technology: Moreauc, Marple B (eds), ASM Int. Materials Park, OH, USA, p 1017
29. Fazilleau J (2003) Understanding of phenomena involved in the production of finely structured coatings by suspension plasma spraying PhD. Thesis (in French), University of Limoges
30. Vattulainen J, Hämälainen E, Hernberg R, Varisto P, Mäntyla T (2001) J Therm Spray Technol 10:94
31. Heberlein J (1999) In: Fauchais P, van der Mullen J, Heberlein J (eds) Heat and mass transfer under plasma conditions, Annals of the New York Academy of Sciences, p 14

32. Lagnoux O, Coudert JF, Wittmann K, Fauchais P (2000) In: Berndt cc (ed) Thermal spray: surface engineering via applied research, ASM Int. Materials Park, OH, USA p 71
33. Döring JE, Vaßen R, Stöver D (2003) In: Moreau C, Marple B (eds) Thermal spray 2003: advancing the science and applying the technology, ASM International, Materials Park, OH, USA, p 641
34. Hwang SS, Liu Z, Reitz RD (1996) Atomization Sprays 6:353
35. Fauchais P, Elchinger MF, Aubreton J (2000) J High Temp Mat Process 4:21
36. Delluc G, Perrin L, Ageorges H, Fauchais P, Pateyron B (2004) In: Proceedings of ITSC 2004, DVS, Düsseldorf, Germany (electronic version)
37. Spalding B (1977) Genmix, Pergamon Press, London
38. Delluc G, Ageorges H, Pateyron B, Fauchais P (2005) J High Temp Mat Process 9:211
39. Betoule O (1995) Ph.D Thesis (in French), University of Limoges, France
40. Planche MP (1995) Ph.D Thesis (in French), University of Limoges, France
41. Coudert JF, Chazelas C, Rigot D, Rat V (2005) J High Temp Mat Process 9:173
42. Pfender E (1989) Plasma Chem Plasma Process 9:167S
43. Borgianni C, Capitelli M, Cramarossa F, Tricolo L, Molinari L (1969) Combustion Flame 13:181
44. Chen X, Pfender E (1958) Plasma Chem Plasma Process 5:119